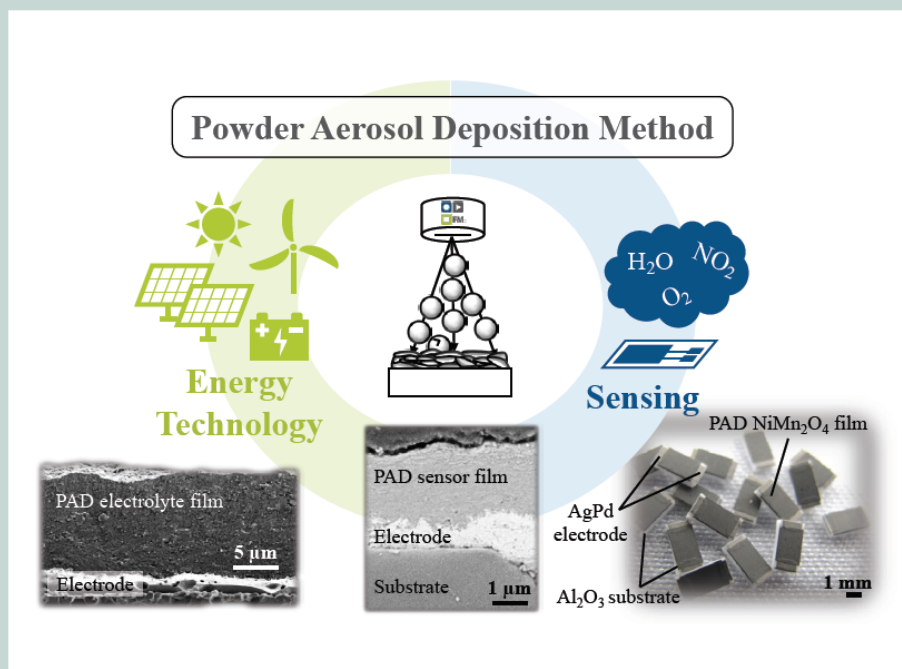


# FUNCTIONAL MATERIALS LETTERS

Volume 12 · Number 5 · October 2019

Editor-in-Chief  
Li Lu

Associate Editors  
Andreas Rüdiger  
Rüdiger-A. Eichel  
Yinong Liu



## Powder aerosol deposition method — novel applications in the field of sensing and energy technology

Michaela Schubert, Dominik Hanft, Tobias Nazarenus, Jörg Exner,  
 Michael Schubert, Philipp Nieke, Philipp Glosse, Nico Leupold,  
 Jaroslaw Kita and Ralf Moos\*  
*Department of Functional Materials*  
*University of Bayreuth*  
*Universitätsstraße 30*  
*D-95447 Bayreuth, Germany*  
 \**Functional.Materials@uni-bayreuth.de*

Received 7 July 2019; Accepted 27 July 2019; Published 22 August 2019

The Aerosol Deposition (AD) method is a dry spray coating process for the production of dense ceramic coatings at room temperature directly from the ceramic raw powder. In order to avoid confusion with liquid aerosol technology, the term powder aerosol deposition (PAD) is introduced here, to highlight that the aerosol consists only of ceramic powder and carrier gas. Especially in the field of functional ceramics, PAD is a promising alternative to conventional sinter-based production processes. This review focuses on the PAD of functional ceramics in the field of sensing and energy technology. In this context, especially current developments and trends are presented. On the part of the sensors, gas and temperature sensors are especially considered, whereas in the field of energy technology, the focus is on vibration energy harvesting, thermoelectric generators, superconductors, and solar cells as well as on all solid-state batteries and fuel cells. Besides the different applications of PAD films, this review also highlights opportunities for influencing the film properties by the used powder or the process parameters.

*Keywords:* Aerosol deposition method (ADM); ceramic thick films; room temperature process; vacuum cold spraying (VCS); vacuum kinetic spraying (VKS); room temperature impact consolidation (RTIC).

### 1. Introduction

High temperatures, usually above 1000°C, are typically required to produce high-quality ceramic components or films with sufficiently high density.<sup>1,2</sup> Ceramics, especially functional ceramics, which decompose at low temperatures or undergo a phase transformation, can only be produced with considerable effort. In particular, problems such as porosity or incomplete intergranular contact have to be handled. Also, a joining of ceramic films to low-melting substrate materials such as glasses, metals, or polymers is usually not possible. Novel processes are necessary to meet the increased requirements of the ceramics industry in terms of flexibility, integration capability in electronic circuits, and/or miniaturization.

A promising alternative to the established, sintering-based ceramic processes is the aerosol deposition (AD) method, sometimes also referred to as vacuum cold spraying (VCS) or vacuum kinetic spraying (VKS). In order to avoid confusion with liquid aerosol technology, the term “powder aerosol deposition” (PAD) is introduced here. It should highlight that the aerosol consists only of ceramic powders and an appropriate dry carrier gas. The powder AD or PAD is an innovative spray coating process, in which dense ceramic films are produced at room temperature directly from ceramic raw powders.<sup>1–5</sup> Thereby, single powders as well as powder mixtures of ceramic/ceramic,<sup>6–8</sup> ceramic/metal,<sup>9</sup> and ceramic/polymer<sup>10,11</sup> (known as aerosol co-deposition, AcD) can be used.<sup>1</sup> Furthermore, the processing of reactive powders (e.g. moisture, oxygen) is possible. Powder aerosol deposited films typically have film thicknesses from the sub-micrometer to several hundred micrometer range and are characterized by a high density, low surface roughness, an excellent substrate adhesion, and a nanocrystalline film structure.<sup>1,3,4</sup> A summary of the unique features of the powder AD in terms of process and film characteristics is shown in Fig. 1.

---

\*Corresponding author.

This is an Open Access article published by World Scientific Publishing Company. It is distributed under the terms of the Creative Commons Attribution 4.0 (CC BY) License which permits use, distribution and reproduction in any medium, provided the original work is properly cited.

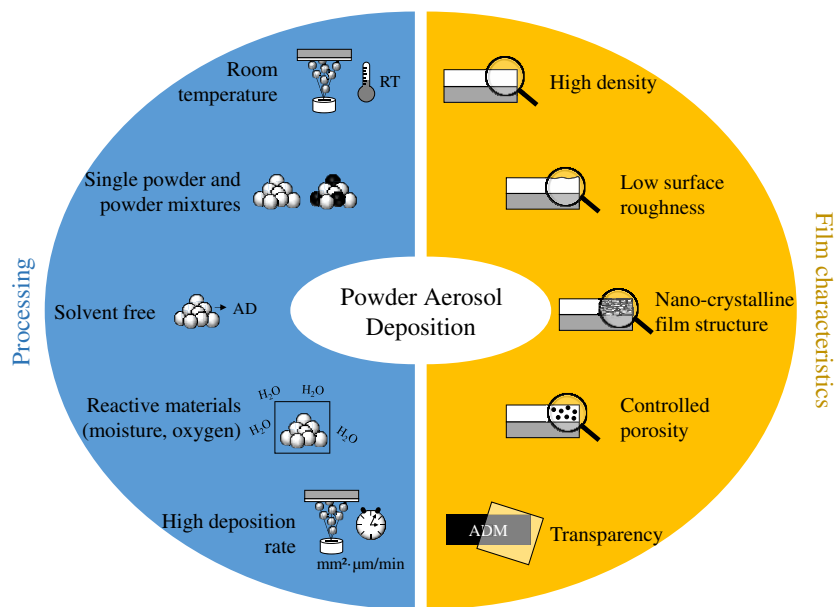


Fig. 1. Unique features of the PAD method.

The film characteristics can differ considerably, which is due to the controllability of the film characteristics by the used powder and the process parameters.

A general prerequisite for successful PAD of mechanically stable films is the optimal correlation between process parameters, powder properties, and substrate characteristics. Due to intensive research in the past years, it is now possible to deposit a large number of ceramic powders on various substrate materials (ceramics,<sup>12,13</sup> metals,<sup>1,14</sup> polymers,<sup>15–17</sup>). Besides familiar ceramics for the AD such as  $\text{Al}_2\text{O}_3$ ,<sup>5,18–20</sup> PZT,<sup>2,17,21</sup>  $\text{BaTiO}_3$ ,<sup>22–24</sup> and  $\text{TiO}_2$ ,<sup>25</sup> further functional ceramics,<sup>26–34</sup> and partly exotic materials, such as lunar regolith,<sup>35</sup> can be deposited today. In addition, more and more powder mixtures are being used.<sup>6,7,36–39</sup> Due to the large variety of ceramic raw powders, powder mixtures and substrate materials, powder aerosol deposited films show diverse properties and thus are used or suggested for many applications these days. In this overview, different applications of powder aerosol deposited film are presented with special focus on the field of sensing and energy technology.

## 2. Setup of a PAD Device and Process Principle

A PAD device typically consists of three main components: a deposition chamber, a vacuum pump and a unit to generate the powder aerosol.<sup>1</sup> Figure 2 shows a schematic setup of a PAD device. A carrier gas (e.g.  $\text{O}_2$ ,  $\text{N}_2$ , or He),<sup>40</sup> is fed into the powder aerosol generation unit. In the powder aerosol generation unit, an aerosol is generated by mixing the carrier gas with the ceramic raw powder using various techniques (e.g. fluid bed or brush generator).<sup>29,41</sup> At the same time, a

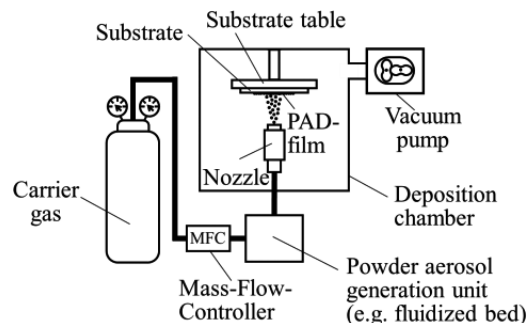


Fig. 2. Scheme of a PAD setup.

constant pressure difference between the aerosol generation unit and the deposition chamber is generated by a vacuum pump.<sup>3</sup> As a result, the generated aerosol is transported into the deposition chamber and is accelerated to a velocity of 100–600 m/s via a nozzle.<sup>1</sup> In the deposition chamber, the particles collide with the substrate and form a firmly adhering ceramic film.

The mechanism of film formation has not yet been conclusively clarified and is only briefly summarized here (for details, see e.g. Hanft *et al.*<sup>1</sup>). It is currently assumed that the film formation takes place in two stages: formation of an anchoring layer and subsequent film buildup.<sup>1,3</sup> The anchoring layer is formed by the first impinging particles deforming the substrate surface and increasing substrate roughness. However, this effect has only been observed on substrate materials such as metals, glasses or polymers, but not on harder ceramic substrates (e.g.  $\text{Al}_2\text{O}_3$ ).<sup>12</sup> The subsequent film formation takes place via fracturing and plastic deformation of the impinging particles, known as Room

Temperature Impact Consolidation (RTIC), proposed by Akedo.<sup>2,3,16</sup> This assumption is supplemented by Lee *et al.*<sup>14</sup> and Exner *et al.*<sup>4</sup> Lee *et al.* attribute the main mechanism of film formation to a kind of hammering effect where the film is densified by subsequent colliding particles.<sup>14</sup> Exner *et al.* postulate the fracturing of crystallites and the generation of fresh and unsaturated surfaces as a prerequisite for successful film formation.<sup>4</sup> For a better understanding of the deposition mechanism, it is also important to know the exact flow conditions during deposition. Accordingly, several studies are currently dealing with flow simulations in the AD process.<sup>42–46</sup>

Successfully deposited films feature an excellent substrate adhesion, a crack- and pore-free film structure as well as properties that are similar to those of classical bulk ceramics. However, the identical functional properties of the bulk ceramics (electric, piezoelectric, dielectric, magnetic) are usually not achieved. Therefore, thermal post-treatment of the films often is conducted. During this process, the film stress decreases, the crystallite size increases or the nanoporosity diminishes, so that bulk properties can be achieved.

### 3. Novel Applications

Based on the large number of oxide and non-oxidic ceramics that have been deposited by means of PAD so far, the number of possible applications of PAD films increases rapidly. Some of these current application trends in the field of sensing and energy technology are presented in Secs. 3.1 and 3.2.

#### 3.1. Sensing

##### 3.1.1. Gas sensors

Powder aerosol deposited films were already used as the main functional component in a variety of gas sensing applications. Up to the year 2015, mainly studies on PAD-based conductometric gas sensors were published. Here, the electrical resistance of the powder aerosol deposited functional film depends directly on the concentration of an analyte in the surrounding gas atmosphere. Examples are oxygen sensing films with a temperature independent characteristics like tantalum-doped barium ferrate ( $\text{BaTi}_{0.7}\text{Ta}_{0.3}\text{O}_{3-\delta}$ , BFT)<sup>47</sup> and heavily iron-doped strontium titanate ( $\text{SrTi}_{0.7}\text{Fe}_{0.3}\text{O}_{3-\delta}$ , STF),<sup>48</sup> as well as composite films of STF and  $\text{Al}_2\text{O}_3$ .<sup>7</sup> When BFT films were operated at a lowered temperature, also hydrocarbons could be analyzed.<sup>47</sup> Hsiao *et al.* demonstrated that ZnO PAD films could be utilized to detect carbon monoxide in the 100–1000 ppm range, however an annealing procedure by laser radiation was necessary.<sup>49</sup> All mentioned sensor application were already summarized in the general overview about PAD from 2015.<sup>1</sup> In recent years, new sensor

technologies emerged in combination with powder aerosol deposited films. While some applications still utilize the conductometric working principle, also capacitive and thermoelectric properties were introduced as gas sensor parameters. A new dynamic measurement method based on alternating voltage pulses (pulse-polarization) was demonstrated for yttria stabilized zirconia films. The ongoing progress in this field is summarized and discussed in this section.

A novel application type for PAD films are humidity sensors. Kumar *et al.* and Liang *et al.* demonstrated that the capacitance of hygroscopic  $\text{BaTiO}_3$  films is highly sensitive to moisture in the air atmosphere.<sup>50,51</sup> Kumar *et al.* investigated also the influence of the electrode geometry and film post-treatment on the sensitivity toward humidity while retaining a constant film thickness of  $1.5\ \mu\text{m}$ .<sup>50</sup> Four different electrode setups were used: three conventional interdigital electrodes (IDE) with varying electrode line widths and one setup with a spiral design. For untreated films, the spiral structure exhibited the highest sensitivity and low hysteresis. A thermal annealing at  $500^\circ\text{C}$  significantly increased sensitivity of the  $\text{BaTiO}_3$  films up to a factor of 80 on all tested electrode setups, possibly due to a slightly increased crystallite size. When annealed, films on conventional IDE with a line width and spacing of  $100\ \mu\text{m}$  become favorable in terms of highest sensitivity and low hysteresis. It was concluded that these films are promising for the application as gas sensors or in the bio-medical field in addition to their humidity sensing properties. Liang *et al.* intensively studied the influence of the film thickness as well as of both microstructure and surface morphology on the resulting humidity sensitivity and response time of  $\text{BaTiO}_3$  AD films.<sup>51</sup> Furthermore, the sensor behavior was described using a comprehensive model also enabling the prediction of the resulting sensitivity. The film morphology is described as a *specific transitional-density* structure where the density gradually changes throughout different layers of the film. Here, the density at the bottom of the film close to the substrate is highest and decreases continuously to the top layer (film surface), as observed by TEM (Fig. 3).

This change in the microstructure was linked to the hammering effect, where subsequently impacting particles consolidate the already deposited film. Consequently, subjacent layers of the film closer to the substrate received intensified hammering with a denser grain arrangement while the top section of the film experienced fewer impacts, featuring more and larger voids as well as larger grains. Films were applied as well on IDE and subsequently annealed at  $400^\circ\text{C}$  for 2 h. Within the investigated thickness range of  $0.1\text{--}10\ \mu\text{m}$ , the  $\text{BaTiO}_3$  films with  $1.5\ \mu\text{m}$  and  $3\ \mu\text{m}$  showed the highest humidity sensitivities (calculated as quotient of capacitance change and relative humidity change within

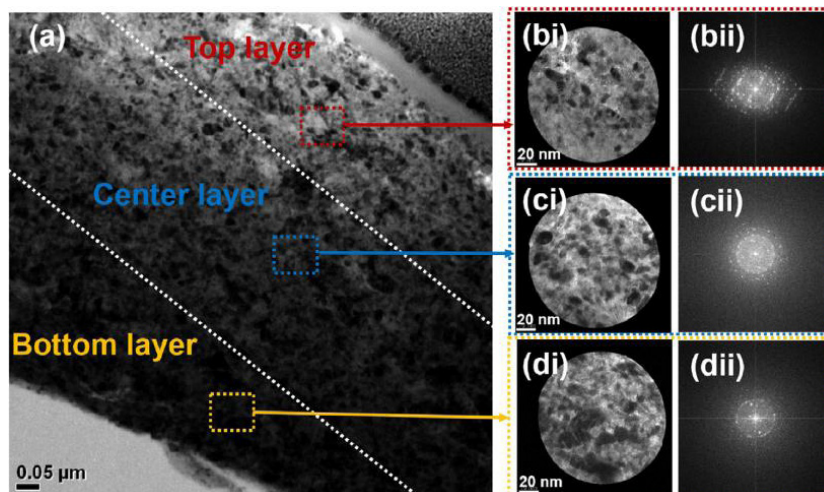


Fig. 3. TEM analysis of a BaTiO<sub>3</sub> AD film. Reprinted from Ref. 51 with permission from Elsevier.

the complete measured range) of 179 (pF/%RH) and 300 (pF/%RH), respectively. All other films outside this narrow range showed significantly smaller sensitivities of 0.1–25 (pF/%RH). Response times were also indirectly dependent on the film thickness, since the (rms) surface roughness and the open-pore ratio are affected. Thicker films with higher surface roughness and increased open-pore ratios exhibited longer response and recovery times, starting from a couple of seconds up to times > 1400 s. Taking all characteristics into account, the 1.5 μm thick film featured high, commercially usable sensitivities in combination with short response and recovery times of 5 s and smaller. The mesoporous microstructure promoted an improved moisture absorption and desorption combined with enhanced detection limits.

In a different approach, *n*-type semiconducting CuO on flexible polyimide (PI) substrates was characterized in respect to its resistive humidity sensing properties.<sup>52</sup> Sensor preparation included the formation of a 200 nm thin (metallic) copper film by nanoparticle deposition (modification of PAD), followed by a low temperature annealing at 250°C in air in order to oxidize the copper to cupric oxide (CuO). In dry conditions, oxygen molecules absorb to the film surface and thereby trap electrons thus increasing the electrical resistance. In humid atmospheres, oxygen bound on the surface is substituted by water molecules, associated with the release of trapped electrons and decrease of the resulting electrical resistance. Produced films exhibited semitransparent properties and a high bending capability. Even after 1000 bending procedures with a bending radius of 0.5 cm, the CuO film is still free of delamination, yet some microcracking is observed. Independent of the bending state, a stable change in electrical resistance of 16–18% occurs when switching between dry (~ 2% RH) and humid (83% RH) conditions. A

response and recovery time of 17.8 s and 5.5 s, respectively, was measured. The authors conclude that this type of sensor could be used as a low cost, metal oxide flexible sensor for various display or window applications. It should be noted that using classical ceramics processing technologies, such CuO layers cannot be deposited, since PI decomposes during firing.

Another new research field are planar capacitive soot sensors based on electrically insulating alumina films, as investigated by Hagen *et al.*<sup>53,54</sup> PAD alumina films exhibit a high electrical resistivity even at elevated temperatures<sup>5,18,19</sup> and are therefore ideally suited for capacitive measurements. Soot is produced in almost all combustions processes, i.e. diesel or gasoline internal combustion engines, and has to be continuously monitored. Dense alumina films were applied directly onto platinum IDE by PAD. Thus, the platinum electrodes are fully embedded without an electrical contact to the surrounding atmosphere. The sensor is additionally equipped with a platinum heater on the reverse side. When electrically conducting soot attaches the surface of the alumina film, the electrical field line distribution changes, leading to an increase in the measured capacitance  $C$  from 10 pF up to 50 pF. Therefore,  $C$  is a suitable measure to monitor the soot loading of the sensor. This sensor is operated in a cycle consisting of two modes: (1) soot loading until a certain amount of soot is attached (a certain value of  $C$  is reached) and (2) thermal regeneration at 600°C to remove the soot and restart the cycle. These sensors were tested with real exhaust gases produced by a diesel engine in an engine test bench. During the 1<sup>st</sup> mode, the soot deposition on the alumina surface is boosted by an applied voltage between 15 V and 180 V at the IDE, leading to shorter blind times until the first change in  $C$  occurs. Higher soot concentration in the tested exhaust gases resulted in a steeper incline of the

capacitance in accordance to the FEM simulations. This indicates that powder aerosol deposited alumina films are suitable for an application as soot sensor even in harsh automotive environments. An advantage of this capacitive soot sensor over conductometric sensors may be a reduced influence of the operating temperature which is of high importance for high dynamic engine operation with widely differing exhaust gas temperatures.

Conventional gas sensors, used to detect and quantify various gaseous components like harmful carbon monoxide or nitrous gases as well as hydrogen or oxygen, were also realized using powder aerosol deposited functional ceramic films. Hanft *et al.* used thin PAD films (1  $\mu\text{m}$  in thickness) of semiconducting tin oxide ( $\text{SnO}_2$ ) in the conductometric operation mode at temperatures in the range between 100°C and 500°C to analyze reducing gases like NO,  $\text{NO}_2$ , CO, and  $\text{H}_2$  with concentrations up to 1000 ppm.<sup>55</sup> In presence of CO and  $\text{H}_2$ , the electrical conductivity increased by two decades, showing an easy-to-measure sensor signal. Responses to NO and  $\text{NO}_2$  are smaller, yet measurable. While at lower sensor operation temperatures below 300°C, the sensitivity toward  $\text{NO}_x$  was predominant, it diminished above 350°C. However, CO and  $\text{H}_2$  responses peaked between 400°C and 450°C. This behavior is beneficial to adjust the sensor to measure especially the intended gases with small cross-sensitivities toward other gaseous components, just by optimizing the operating temperature.

Combined resistive and thermoelectric oxygen sensors with almost temperature-independent characteristics in the range of 600–800°C were realized by Bektas *et al.*<sup>27,56</sup> Films of Al- and Fe-doped barium tantalate ( $\text{BaFe}_x\text{Al}_{0.01}\text{Ta}_{0.99-x}\text{O}_{3-\delta}$ , BFATx) with  $x = 0.1$  and  $x = 0.3$  were tested at oxygen partial pressures  $p\text{O}_2$  between  $10^{-20}$  bar (reducing atmosphere) and  $10^0$  bar (pure oxygen). BFT exhibited a transition from *n*-type behavior at low  $p\text{O}_2$  to *p*-type conduction at high  $p\text{O}_2$ . BFT30 ( $\text{BaFe}_{0.7}\text{Ta}_{0.3}\text{O}_{3-\delta}$ ) was found to be a good candidate as oxygen gas sensor, since its resistivity as well as its thermoelectric Seebeck coefficient exhibited a strong dependency on the oxygen partial pressure, especially between  $10^{-5}$  bar and  $10^0$  bar, while being nearly independent on the operating temperature. The used measurement setup of this initial study was restricted in terms of the measuring frequency. As a result, response times of several minutes occurred that are still too long for many practical applications.

Besides these conventional approaches with a resistive or capacitive sensor mechanism, also highly dynamic methods could be adapted to PAD films.<sup>26</sup> An example is the nitrogen oxide ( $\text{NO}_x$ ) sensor based on the pulse-polarization method. This technique is usually applied to commercially available thimble-type lambda probes and can be used to detect small

concentrations of  $\text{NO}_x$  in the ppm range. The mechanism involves alternating polarization pulses of an oxide ion conducting membrane (like 8YSZ) equipped with platinum electrodes, interrupted by self-discharge pauses. The amount of  $\text{NO}_x$  within the surrounding atmosphere significantly affects the course (rate) of self-discharge, even when only sub-ppm concentration are present. Exner *et al.* used a miniaturized sensor with a planar setup consisting of an aerosol deposited 8YSZ film on an alumina substrate and screen printed and sintered platinum IDE, considerably smaller than thimble-type lambda probes. A sensor temperature of 425°C enabled the quantitative detection of NO,  $\text{NO}_2$ , and mixtures of both for small concentrations of 3–48 ppm. High sensor output voltages of 50–300 mV with small noise were observed, that could be easily measured. When the 8YSZ films were produced by screen-printing instead of PAD, the sensitivity toward  $\text{NO}_x$  reduces and the noise increases, again underlining the great potential of PAD to produce functional ceramic films. Another interesting finding is the decrease in sensitivity toward NO when the sensor is operated in a unidirectional pulse mode instead of alternating pulses. Since the sensitivity of  $\text{NO}_2$  is not affected, a mixed operation mode periodically switching between alternating and unidirectional pulses was suggested. Here, a simultaneous determination of the NO and  $\text{NO}_2$  may become possible.

PAD offers a high variety and potential to produce functional sensor components, as described by the prior examples. The high integrity and adhesion of aerosol deposited films in combination with near bulk-like functional properties provides benefits for ceramic gas sensors.

### 3.1.2. Temperature sensors

Also in the field of ceramic temperature sensors based on negative temperature coefficient thermistor materials, PAD is a promising alternative to conventional sinter-based manufacturing processes.<sup>1</sup> Thus both Ryu *et al.*<sup>57,58</sup> and Baek *et al.*<sup>59</sup> showed that it is possible to deposit a spinel-based  $\text{NiMn}_2\text{O}_4$  raw powder into dense films (no pores or cracks) with excellent substrate adhesion. The films are characterized by a nanocrystalline film structure and the typical NTCR behavior, i.e. they show an almost exponential decrease of the electrical resistance  $R$  with increasing temperature. It was also noticed that the characteristic NTCR parameters (specific resistance at 25°C  $\rho_{25}$  and thermistor constant  $B$ ) are slightly higher than those of conventionally sintered components but can be reduced by subsequent film tempering. In addition, Ryu *et al.*<sup>60</sup> showed that the temperature sensitivity of the PAD-NTCR film could be improved by doping the  $\text{NiMn}_2\text{O}_4$  powder with Co or both Co and Fe. In this way, mechanically stable PAD films with a  $B$  value above 5600 K could be produced. A further modification of the NTCR

characteristic was possible by depositing a  $\text{NiMn}_2\text{O}_4$  powder with dispersed conductive  $\text{LaNiO}_3$  particles, as described in Kang *et al.*<sup>61</sup> Besides the dense film structure and the excellent substrate adhesion, the PAD films also showed a higher temperature sensitivity ( $B$ -value).

In the past few years, the development of ceramic NTC thermistors has focused primarily on two approaches. First, the existing approach of PAD of a completely processed powder has been further developed. Jung *et al.* showed that the PAD of perovskite-based  $\text{YBa}_2\text{Cu}_3\text{O}_{6+x}$  powders to mechanically stable films with typical NTCR characteristics is also possible.<sup>62</sup> Schubert *et al.* carried out further investigations on the PAD of spinel-based  $\text{NiMn}_2\text{O}_4$  ceramics.<sup>30,63,64</sup> Besides the development of chip-based components (see Fig. 4),<sup>63,64</sup> these authors were focusing on tempering<sup>30,63</sup> and aging<sup>63</sup> of NTCR films. They attributed the known tempering effect to a reduction of microstrain and crystallite growth and showed a significant improvement in aging stability. Films tempered at  $400^\circ\text{C}$  exhibit higher aging stability than conventionally sintered  $\text{NiMn}_2\text{O}_4$  bulk ceramics.<sup>63</sup>

In the second approach, a thermally untreated powder mixture of the starting oxides is deposited and the deposited films are then thermally treated (*in situ* calcination<sup>38</sup>). It was shown that mechanically stable films with cubic spinel structure and typical NTCR characteristics can be produced by powder aerosol co-deposition of a  $\text{NiO-Mn}_2\text{O}_3$  powder mixture followed by an *in situ* calcination of the composite films.<sup>38</sup> The authors also developed a novel process, in which the approach of powder aerosol co-deposition with subsequent *in situ* calcination is combined with the sintering of screen-printed electrodes.<sup>39</sup> The advantage of this approach is only one single temperature treatment at  $850^\circ\text{C}$  is required to produce mechanically stable NTCR sensors with the same  $\rho_{25}$ - and  $B$ -values as classically sintered bulk ceramics.

Due to the possibility to produce fully dense and mechanically stable films with typical NTCR characteristics by PAD or by AcD with subsequent *in situ* calcination, both approaches are very interesting for a possible utilization in NTC thermistor applications. Especially the absence of the

complex sintering step above  $1000^\circ\text{C}$  simplifies the process (no problems with porosity or material decomposition<sup>65–67</sup>) and saves energy.

### 3.2. Energy technology

In addition to the sensor field, applications of PAD films in energy technology are currently in vogue. In the following, some new findings in the fields of vibration energy harvesting, thermoelectric generators (TEGs), superconductors, solar cells as well as batteries and fuel cells are overviewed.

#### 3.2.1. Vibration energy harvesting and actuation

The unique feature to produce high-density ceramic films at room temperature also motivates the application of the PAD method for piezoelectric materials.<sup>2,68</sup> Due to its superior piezoelectric properties, especially  $\text{Pb}(\text{Zr,Ti})\text{O}_3$  (PZT) has been object under investigation.<sup>68</sup> The requirement of large grain sizes ( $> 1\ \mu\text{m}$ ) for high piezoelectric activity is, however, in strong contrast to the typical nanocrystalline and amorphous microstructure of PAD films.<sup>1,69</sup> Therefore, deposited films are usually heat-treated to promote grain growth.<sup>68,70,71</sup> Conventional annealing limits the selection of substrate materials to chemical inert materials with a high thermal stability.<sup>71</sup>

Approaches to overcome this challenge include laser annealing or separation of the deposited films from the original substrate. Palneedi *et al.* used a continuous-wave ytterbium fiber laser (560 nm, approximately  $50\ \mu\text{m}$  effective beam size) to locally anneal PZT-films on heat sensitive amorphous Metglas foils (FeBSi) by raster scanning.<sup>72,73</sup> Hwang *et al.* described a technique called inorganic-based laser lift-off (ILLO) to separate PAD films from their original substrates.<sup>74</sup> Deposition and conventional annealing in a furnace have been conducted on the high melting sapphire substrate. Subsequently the film has been separated by irradiating the reverse side of the sapphire substrate with a XeCl excimer laser (308 nm, photon energy of 4.03 eV). Because of the wide band gap of sapphire (10 eV), the energy initially couples in the interface between PZT and sapphire and locally vaporizes the PZT material (band gap energy 3.3 eV).<sup>75–77</sup> After separation, the PZT film has been attached to a flexible polyethylene terephthalate (PET) substrate.

Akedo *et al.* emphasize the main advantages of piezoelectric systems for vibration energy harvesting. They include low cost, compact design, and the potential to realize wearable structures.<sup>2,78</sup> Recent works propose the benefits of piezoelectric PAD films for energy harvesting. Especially the utilization for wireless sensing applications seems to be promising.<sup>21</sup> Vibration energy harvesting devices based on cantilever beams (unimorph or bimorph structure) have been

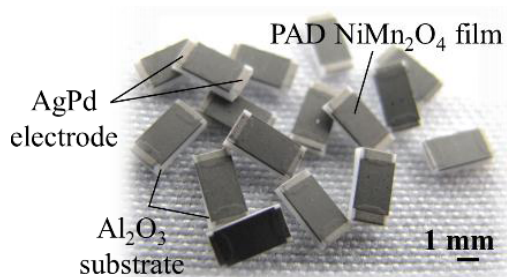


Fig. 4. NTC thermistor devices consisting of an alumina substrate, AgPd screen-printing electrodes and an AD  $\text{NiMn}_2\text{O}_4$  film.

reported.<sup>2,21</sup> Here, an oscillating weight (seismic mass) on the tip of a cantilever beam deforms a piezoelectric layer periodically in order to generate an output voltage. For example, a maximum power output of  $423\ \mu\text{W}$  at an excitation frequency of 143.4 Hz and excitation acceleration of 1.5 g for a bimorph structure ( $9 \times 6 \times 0.09\ \text{mm}^3$ ) has been achieved by Kuo *et al.*<sup>21</sup> On the contrary, the composite structure from Hwang targets lower frequencies.<sup>79</sup> In a long-term test encompassing 115,000 bending cycles an open-circuit voltage of 75 V and short-circuit currents of  $14\ \mu\text{A}$  at a frequency of 0.4 Hz have been achieved.

Actuators are another field of application for powder aerosol deposited piezoelectric layers. Two possible applications were mainly investigated in scientific papers. These are on the one hand optical microscanners<sup>2,80–82</sup> and on the other hand piezoelectric micromachined ultrasonic transducers (pMUT).<sup>2,83</sup> Regarding the optical microscanners, two different substrate materials were used: silicon wafer and stainless steel. On the Si wafer, a  $6\ \mu\text{m}$  thick PZT film was deposited and annealed at  $600^\circ\text{C}$  for 1 h. With this device, a scanning angle of  $25.9^\circ$  was achieved, using a driving voltage of 60 V and a resonance frequency of 33 kHz.<sup>80</sup> The scanners made on stainless steel could reach similar values. Using PAD-PZT films with a thickness between  $5\ \mu\text{m}$  and  $20\ \mu\text{m}$  (also annealed at  $600^\circ\text{C}$  for 1 h), a scanning angle up to  $41^\circ$  was possible, with a driving voltage of only 60 V and a resonance frequency at roughly 20–30 kHz.<sup>81,82</sup> By adjusting the mirror size and hinge length, the scanning frequency and angle could easily be tailored.

Another reported application field of a piezoelectric actuator device is a pMUT.<sup>83</sup> For this ultrasonic transducer, an  $8\ \mu\text{m}$  thick PZT film was deposited via Granule Spray in Vacuum (GSV) on a Pt/Ti/SiO<sub>2</sub>/Si substrate and structured by subsequent processes to produce a membrane with a diameter of  $400\ \mu\text{m}$ . GSV is a derivative of PAD using granulated powder in order to allow stable powder feeding since granules show better flow properties than the primary powder particles. However, at GSV higher speeds are required, as part of the kinetic energy is needed for breaking up the granules before the actual RTIC mechanism occurs. Again, the sample had to be heat-treated at  $600^\circ\text{C}$  to obtain sufficient piezoelectric properties. A displacement of  $0.8\ \mu\text{m}$  was achieved by a driving voltage of only 5 V at a resonance frequency of 300 kHz. By utilizing the GSV for this transducer setup, the most time-consuming step of piezolayer deposition was accomplished within minutes and represents a significant improvement over conventional processes.

### 3.2.2. Thermoelectric Generators (TEGs)

The utilization of TEGs can help to convert excess heat from different processes into electrical energy. TEGs are usually

assembled from bulk materials. The drawbacks of these type of TEGs are low productivity of the bulk process and the high volume of the devices. Film manufacturing techniques show low deposition rates. They need high temperatures and/or the control of the chemical composition is difficult.<sup>84</sup> *P*-type Bi<sub>0.5</sub>Sb<sub>1.5</sub>Te<sub>3</sub> was deposited having a film thickness of  $276\ \mu\text{m}$  and *n*-type Bi<sub>2</sub>Te<sub>2.7</sub>Se<sub>0.3</sub> with  $557\ \mu\text{m}$ . The films showed power factors of  $0.62\ \text{mW/mK}^2$  and  $0.21\ \text{mW/mK}^2$ , respectively, which were comparable to the bulk properties.<sup>84</sup>

The assembly of a TEG by PAD has also been demonstrated.<sup>85,86</sup> Here, *p*-type bismuth antimony telluride is used. Due to its nanocrystallinity, the thermal conductivity is 20–30% reduced compared to bulk samples.<sup>86</sup> As a low thermal conductivity is favorable for a more efficient power generation, this is a benefit of the PAD method. It is reported that with this material  $200\ \mu\text{m}$  thick coatings can even be formed on PET.<sup>85</sup> The maximum output power reported in this publication is about  $54\ \mu\text{W}$ .

Materials to prepare thermoelectric sensors are also mentioned in the section *sensing*. As an example, the delafossite copper iron oxide (CuFeO<sub>2</sub>) owns a high Seebeck coefficient and is therefore also a promising thermoelectric material.<sup>87</sup> Depending on the oxygen partial pressure this material can be used in the *p*- or *n*-type state. The RTIC process can reduce the grain size, leading to a lower thermal conductivity which has a positive impact on the thermoelectric performance. Nevertheless, the power factor is lower compared to bulk samples.<sup>33</sup> The reason is yet unclear.

### 3.2.3. Superconductors

The possibility to produce superconducting coatings, especially of magnesium diboride (MgB<sub>2</sub>), via PAD has already been mentioned several years ago by Akedo *et al.*<sup>88</sup> Since then, several studies investigating this material class have been published.<sup>29,89–92</sup> State-of-the-Art to prepare films, bands, or wires of MgB<sub>2</sub> are the so-called powder-in-tube-technique magnesium diffusion method and the conventional physical vapor deposition.<sup>90</sup> Both techniques need either a well-aligned atmosphere or high temperatures. A successful production of long tapes has not been reported up to now. As indicated by Arndt,<sup>93</sup> the PAD method may overcome this due to its capability as a reel-to-reel manufacturing process. Since MgB<sub>2</sub> is nearly isentropic and has a large coherence length,<sup>94</sup> it is thought to be appropriate to be used as a polycrystalline PAD-film. A critical current density of  $J_C \approx 5\ \text{kA/cm}^2$  (at 4.2 K, 0 T) was achieved by Kauffmann-Weiss *et al.*<sup>90</sup> They also report a critical temperature  $T_{C0}$  of 18.1 K for these films.<sup>90</sup> The average thickness of MgB<sub>2</sub> films can be in the range of 70–100  $\mu\text{m}$ . Due to stresses in the film and the high amount of amorphous regions in PAD films, the transition temperature is reduced and the transition

width is increased compared to bulk samples prepared from the same precursor powder.<sup>91,92</sup> A heat treatment of  $\text{MgB}_2$  PAD-films leads to a better intergrain connectivity and the  $T_C$  is enhanced as well as the transition width is reduced.

### 3.2.4. Solar cells

Depending on the optoelectronic material system, many processes for solar cell fabrication suffer from low deposition rates, coupling of material synthesis and film formation and/or from poor suitability for large area production. For instance, an established alternative to silicon-based solar cells are copper indium gallium selenide (CIGS) solar cells, which are often co-evaporated or sputtered onto a heated substrate.<sup>95</sup> Characteristic for the process is the need for a high vacuum (very low pressures) and slow deposition rates making the production expensive.

Park *et al.* simulated the deposition of  $\text{CuInGaSe}_2$ -particles onto Mo-substrates to optimize the deposition process for this material system.<sup>96</sup> Their results suggest a rather low particle velocity of maximum 200 m/s to avoid substrate damage that would lead to a poor electrical connection to the back contact. Their simulations also indicate local temperatures of 1000 K which would allow local sintering. In a following study,  $\text{Cu(In, Ga)(S,Se)}_2$  solar cells made by PAD with a conversion efficiency of up to 5.5% are demonstrated for the first time.<sup>97</sup> However, they had to use various post-treatment steps to remove oxygen incorporated by spraying with dry air and to increase film quality and crystal size. An SEM image of an improved CIGSse-film for solar cell fabrication is shown in Fig. 5.

The emerging lead-halide perovskite solar cells with the archetypical methylammonium lead (II) iodide ( $\text{CH}_3\text{NH}_3\text{PbI}_3$ , MAPbI) are usually processed on solution basis, for instance

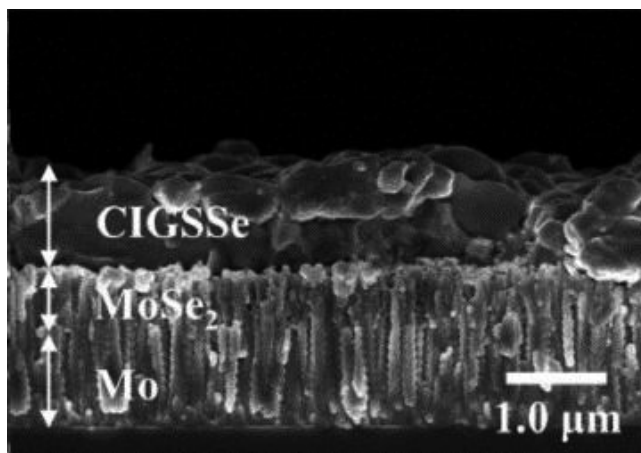


Fig. 5. Improved CIGSse-PAD-film for fabrication of solar cells with efficiencies of 5.49%. Reprinted from Ref. 97 with permission from Elsevier.

by spin coating or by co-evaporation.<sup>98</sup> Both techniques have in common that they couple perovskite synthesis and film formation. This makes film formation hard to control and complicates fine-tuning of film properties. In contrast to that, the PAD method allows for decoupling material synthesis from film formation by first manufacturing and optimizing a hybrid perovskite powder, e.g. mechanochemically in a ball mill,<sup>99</sup> which can then serve as the powder for the PAD process. Therefore, Panzer *et al.* deposited MAPbI onto  $\text{TiO}_2$  coated glass substrates. The perovskite structure and optical properties of MAPbI are transferred from the powder to the film paving the way for a solvent-free synthesis route.<sup>32</sup>

Before the rise of perovskite solar cells PAD of dye sensitized solar cells components (DSSC) were an intensively researched field. For that purpose, the PAD of  $\text{TiO}_2$  as an electron extraction layer has been extensively studied. An overview on the deposition of  $\text{TiO}_2$  for DSSC can be found in Hanft *et al.*<sup>1</sup>

### 3.2.5. Batteries

Applications for the PAD process can be found in every field, where its unique features (see Fig. 1) provide advantages compared to the current state of the art in process technology. This situation can be found in the field of battery production. The future demand for storage capacity driven by electromobility will exceed the current capacities many times over. The present research on lithium batteries aims on finding new ways to increase energy and power density of battery cells and stacks, which seems to require a rigorous change in materials and process technology. Several studies predict a “solid future” for the battery<sup>100,101</sup> since all-solid-state battery (ASSB) architectures might enable new anode (lithium metal) and cathode materials (high voltage material and high capacity materials) with high energy density by replacing liquid electrolytes with solid electrolytes (SEs), e.g. ceramic lithium ion conductors. Different film forming process technologies such as tape casting, screen-printing and extrusion are worth to be considered for fabrication of such cells.<sup>102,103</sup>

Promising concepts on ASSBs see lithium metal (approximately 3860 mAh/g) as potential anode material. Apart from lithium metal, different kinds of anode materials such as  $\text{TiNb}_2\text{O}_7$  (TNO),<sup>104</sup>  $\text{Li}_4\text{Ti}_5\text{O}_{12}$  (LTO)<sup>105</sup> were deposited by PAD and tested concerning their cycling behavior. However, especially when using lithium metal as anode material, the dense structure of the SE is necessary in order to prevent from dendrite shortening of the cell. Ceramic or glass-like  $\text{Li}^+$  conductors can be used to provide a high ionic conductivity as SE and to guard the anode from a composite cathode of e.g. NCM (Fig. 6).

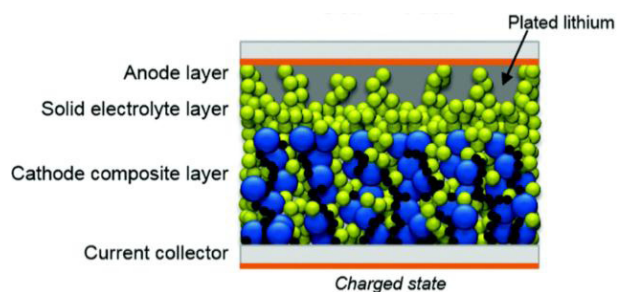


Fig. 6. Schematic of an ASSB cell of composite cathode, SE, and Li-metal anode. Reprinted from Ref. 103 with permission from RSC Publishing.

Considering the described ASSB architecture, the AD process might have certain tremendous advantages for all different cell components. In the following, we will discuss some ideas of PAD application.

To achieve high energy densities, both mass and volume of passive components like e.g. the SE, have to be kept small. This means light materials are favorable.<sup>106</sup> In general, materials with high ionic and low electronic conductivities are relevant. The aim is to achieve homogeneous, dense, and flawless membranes in the  $\mu\text{m}$ -thickness-range with sufficient mechanical stability at the same time. A variety of SE materials was already shown to be processable as dense and  $\mu\text{m}$ -thick films by PAD, e.g. phosphates as  $\text{Li}_{1.7}\text{Al}_{0.3}\text{Ti}_{1.7}(\text{PO}_4)_3$  (LATP or LAGP),<sup>107–109</sup> titanates ( $\text{Li}_{0.35}\text{La}_{0.55}\text{TiO}_3$ , LLT),<sup>110</sup> or garnet-type structures ( $\text{Li}_7\text{La}_3\text{Zr}_2\text{O}_{12}$ , LLZO).<sup>31,111,112</sup> Although the crystal phases of the deposited materials remain unchanged, usually severe lattice distortion and nanocrystallinity (they stem from the RTIC mechanism-related particle fracture) reduce the ionic conductivity. By a thermal post-processing, the original electrical bulk properties may be recovered.<sup>31,108</sup> Compared to conventional sinter processes, the much lower recovery temperatures are beneficial. This is a general advantage of the PAD process.<sup>3</sup>

Switching from common liquid  $\text{Li}^+$ -ion cells to ASSB has major consequences on the cathode side. Deposition of cathode films of several  $\mu\text{m}$  thickness was shown for  $\text{LiMn}_2\text{O}_4$ ,<sup>113</sup>  $\text{LiNi}_x\text{Co}_y\text{Mn}_z\text{O}_2$ ,<sup>114,115</sup>  $\text{LiFePO}_4$ <sup>112,116,117</sup> and  $\text{LiV}_3\text{O}_8$ ,<sup>118</sup> although, considering high energy cells, the thickness of the cathode layer has to be increased.<sup>106</sup> However, it becomes even more complicated, since besides the storage component, solid ion- and electron-conducting components are necessary. All components need to be dispersed homogeneously in order to guarantee high charge and discharge current densities (Fig. 6). Several examples proved that mixtures can be deposited with homogeneous dispersion and intimate contact in general.<sup>119</sup> This could provide additional advantages, since there is no need for binder additives to achieve stable composite films.

However, the distortion of the crystal structure turns out to be a major issue that results in a decay of the electrochemical

behavior of the films: An annealing post-treatment of films turns to be difficult, due to a possible interdiffusion and corresponding degradation of interfaces between the different materials like e.g. NCM and LLZO in the composite cathode.<sup>120,121</sup> Considering this, it would be preferable to control the crystallinity in the film by controlling the PAD process parameters. Since the densification of the film relies on fracture and deformation of the particles, one of the effects (a full densification or preservation of initial crystallinity) would be impeded. However, it might be possible to control this effect by a certain degree through variation of the kinetic energy of the particles, e.g. by the carrier gas flow,<sup>3,122</sup> species,<sup>3,40,123,124</sup> and nozzle design.<sup>125</sup> Furthermore, particles size and distribution of powder mixtures can decide over the final film properties. Studies show that agglomerates of nano-sized primary particles show a negligible reduction in particle and crystallite size after deposition, which is expressed in an unchanged width of diffraction reflexes of the films compared to the initial powder.<sup>105</sup> The resulting electrochemical properties remain (mostly) unchanged. As another attempt, consolidated films with less strain and microstructural distortion could be created by the co-deposition of different materials. This can generate interesting composite microstructures as shown for the nanoparticle deposition (NPD) process in Fig. 7.<sup>126</sup>

Among others, the effect can be caused by the different powder particle sizes. Besides that, it can also be achieved by embedding a harder fraction into a softer material.<sup>6</sup> Up to now, this effect has not been shown for battery materials yet.

Finally, as there are several examples to fabricate the individual functional components by PAD, one should also consider the direct processing of subsequent components of a battery cell e.g. by the direct deposition of the cathode on the SE or vice versa as well as the deposition of gradients through subsequent deposition of different materials mixtures.<sup>127</sup>

In comparison to high-temperature processes that will lead to significant diffusion of elements between the different components of the cathode,<sup>128</sup> PAD offers a valuable alternative due to the room temperature process conditions. This can prevent from reaction and deliver intimate contact between the different components. However, effects such as diffusion that might arise from an additional annealing treatment even at reduced temperatures to recover the functional properties have to be taken into account. The described process can indeed reduce the temperature for setting the coating properties. Ultimately, however processing of components might not be possible without any thermal post-treatment.

As mentioned in this section, the PAD process gives a variety of opportunities to process the different components of a future ASSB. The versatility of the process results from

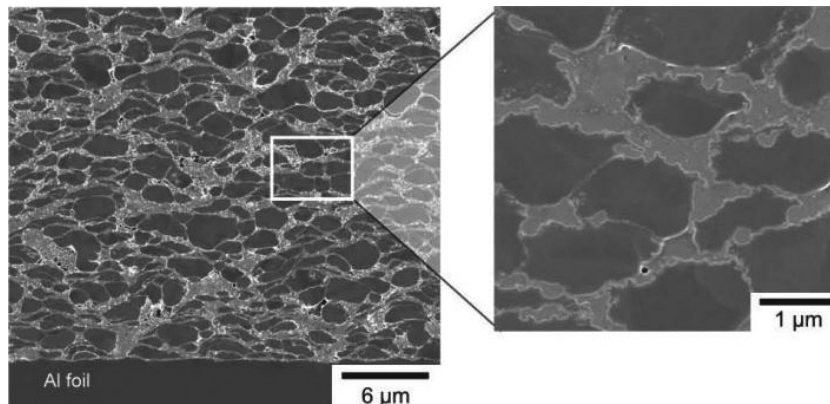


Fig. 7. Composite films processed by NPD system. Embedded aluminum particles in a matrix of BaTiO<sub>3</sub>. Reprinted from Ref. 126 with permission of the authors.

the targeted variation of the process parameters such as particle size distribution, co-deposition, and particle energy during deposition.

### 3.2.6. Fuel cells

Fuel cells are an alternative way to convert chemical into electric energy. High-temperature solid oxide fuel cells (SOFCs) are not only for energy generation through the recombination of hydrogen and oxygen but also for the conversion of common hydrocarbon fuels and thus for forming an ideal transition technology (e.g. for decentralized energy supply). The core of that fuel cell-type is a ceramic electrolyte that conducts oxide ions (e.g. yttria-stabilized zirconia, YSZ), whereby proton-conducting ceramic electrolytes are currently also under investigation, since one envisages reduced operating temperatures of only approximately 700°C. As mentioned in the battery section, one of the major challenges in the operation of SOFCs are temperature-related interdiffusion processes. They can occur during co-sintering processes of the components during cell production, but also during (high temperature) operation. In particular, insulating intermediate phases (e.g. SrZrO<sub>3</sub> and La<sub>2</sub>Zr<sub>2</sub>O<sub>7</sub>) are formed between the cathode (e.g. LSCF) and the electrolyte (e.g. YSZ). They reduce the cell performance and hinder its commercial realization. One way to meet this challenge is to introduce diffusion barrier layers between the electrolyte and the cathode to prevent this kind of cell aging. These protective layers mostly consist of gadolinium- or samarium-doped cerium oxide (1). Another conceivable option is to reduce the processing temperatures. This can also go hand-in-hand with the choice of other electrolyte materials (2). The PAD method at room temperature is predestined for both approaches.

(1) By PAD, flawless ceramic coatings on the SE can be produced. The requirements for the powder already have been investigated. Even if particles with a particle size of

approximately 2 μm are required for the PAD process,<sup>28,129</sup> layers with a thickness of approximately 1.5 μm<sup>130</sup> (see Fig. 8) can be produced due to the impact-based consolidation process of the particles.<sup>3</sup> The layers have a high adhesive strength and are gas-tight. In addition, it has already been proven that the cathode could be built up on the PAD-processed protective layers by screen-printing and that functional cells could be produced.<sup>131</sup>

(2) In addition to the formation of diffusion barrier layers to allow high-temperature operation, SEs can be directly deposited on porous electrodes.<sup>132</sup> In order to kinetically prevent interdiffusion during operation, it is necessary to lower the operating temperature of the fuel cell. Further adjustments are necessary to ensure that the performance does not drop, since YSZ conducts ions significantly lower at lower temperatures. This can be achieved by alternative electrolyte materials with sufficient conductivities at lower temperatures, e.g. some proton-conducting ceramics (barium stannates, barium cerates, or barium zirconates). Another approach is to significantly reduce the electrolyte layer thickness and thus the oxide diffusion length (< 15 μm) as one major contributions to

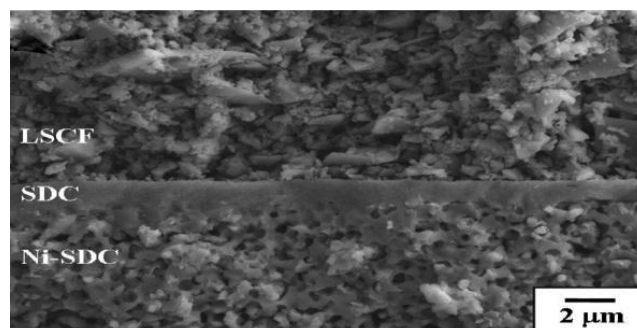


Fig. 8. Powder aerosol deposited Sm<sub>0.2</sub>Ce<sub>0.8</sub>O<sub>2</sub> film. Reprinted from Ref. 130 with permission from Elsevier.

the overall cell-resistance. In that case, the mechanical stability of the cell must be provided by other components (electrode or interconnector).

In principle, the structure of the porous electrodes is also conceivable. As already shown, the co-deposition of several powders is also possible. If a soluble/combustible second component (e.g. a polymer) is selected, a porous PAD electrode-layer can also be produced in a subsequent step.

#### 4. Summary

This small review deals with current trends and developments in the field of PAD of functional ceramics for applications in the field of sensing and energy technology. It is shown that PAD offers an enormous potential for various applications in the field of gas and temperature sensors, as well as for vibration energy harvesting and actuation, TEGs, superconductors, solar cells, batteries, and fuel cells. This potential is based on the unique features of the PAD. Various features offer ample advantages over the state-of-the-art coating techniques like physical vapor deposition (PVD), chemical vapor deposition (CVD), chemical solution deposition (CSD), screen-printing and thermal spraying for functional ceramics. From the side of process technology (left-hand side in Fig. 1), processing at room temperature, high deposition rates, or solvent-free processing have to be mentioned. As shown in Fig. 9, the heat loading on the substrate during PVD processes, such as vaporization or sputtering, is similarly low. However, the deposition rate of the PAD processes is about 30 times higher than for PVD or CVD processes.<sup>3</sup> All other processes take place at higher substrate temperatures (CVD) or require a thermal treatment for solvent removal (CSD) or for film sintering (screen-printing).

Compared to PAD, thermal spraying or screen-printing achieve significantly higher deposition rates. However, the surface roughness and the film density (pores, cracks) are usually higher, too.<sup>3,133,134</sup> Changes in the composition or oxidation state of the functional ceramics can also occur during thermal spraying, screen-printing or PVD processes.<sup>134</sup> This

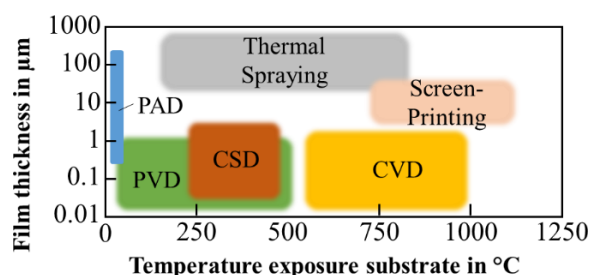


Fig. 9. Comparison of different coating techniques for functional ceramics.<sup>3,133,134</sup>

is different with the PAD process. In this process, films with high density, transparency or controlled porosity can be produced without any change in composition, stoichiometry or crystal structure. Consequently, the PAD process is also advantageous from the side of film characteristics in many applications.

In future, the process of the PAD could play an increasingly important role for functional ceramics when applied in the field of sensing and energy technology.

#### References

1. D. Hanft *et al.*, *J. Ceram. Sci. Technol.* **6**, 147 (2015).
2. J. Akedo *et al.*, *Jpn. J. Appl. Phys.* **57**, 07LA02 (2018).
3. J. Akedo, *J. Therm. Spray Technol.* **17**, 181 (2008).
4. J. Exner *et al.*, *J. Eur. Ceram. Soc.* **39**, 592 (2019).
5. M. Schubert *et al.*, *Mater. Lett.* **245**, 208 (2019).
6. J. Exner *et al.*, *J. Am. Ceram. Soc.* **98**, 717 (2014).
7. J. Exner *et al.*, *Sens. Actuators, B* **230**, 427 (2016).
8. K. Yuuki *et al.*, *Key Eng. Mater.* **582**, 141 (2013).
9. J.-H. Park *et al.*, *Jpn. J. Appl. Phys.* **45**, 7512 (2006).
10. S. H. Cho *et al.*, *J. Korean Phys. Soc.* **68**, 340 (2016).
11. S. H. Cho *et al.*, *Ceram. Int.* **38**, 131 (2012).
12. M. Schubert *et al.*, *Funct. Mater. Lett.* **10**, 1750045 (2017).
13. J. Exner *et al.*, *Adv. Powder Technol.* **26**, 1143 (2015).
14. D.-W. Lee *et al.*, *J. Am. Ceram. Soc.* **94**, 3131 (2011).
15. J. Ryu *et al.*, *J. Am. Ceram. Soc.* **92**, 524 (2009).
16. J. Akedo, *J. Am. Ceram. Soc.* **89**, 1834 (2006).
17. B. Ma *et al.*, *Mater. Sci. Energy Technol.* **2**, 96 (2019).
18. N. Leupold *et al.*, *Funct. Mater. Lett.* **11**, 1850022 (2018).
19. M. Schubert *et al.*, *J. Therm. Spray Technol.* **17**, 870 (2018).
20. O.-Y. Kwon *et al.*, *J. Ceram. Process. Res.* **19**, 290 (2018).
21. C.-L. Kuo *et al.*, *Smart Mater. Struct.* **25**, 105016 (2016).
22. N. H. Khansur *et al.*, *Ceram. Int.* **44**, 16295 (2018).
23. N. H. Khansur *et al.*, *Scr. Mater.* **157**, 86 (2018).
24. J.-G. Liang *et al.*, *ACS Appl. Mater. Interfaces* **10**, 851 (2018).
25. J. Adamczyk *et al.*, *Surf. Coat. Technol.* **350**, 542 (2018).
26. J. Exner *et al.*, *Sensors* **17**, 1715 (2017).
27. M. Bektas *et al.*, *J. Sens. Sens. Syst.* **7**, 289 (2018).
28. J. Exner *et al.*, *Materials* **11**, 2072 (2018).
29. D. Hanft *et al.*, *Materials* **11**, 1572 (2018).
30. M. Schubert *et al.*, *J. Eur. Ceram. Soc.* **38**, 613 (2018).
31. D. Hanft *et al.*, *J. Power Sources* **361**, 61 (2017).
32. F. Panzer *et al.*, *Materials* **9**, 277 (2016).
33. T. Stöcker *et al.*, *Materials* **9**, 227 (2016).
34. J. Exner *et al.*, *Thin Solid Films* **573**, 185 (2014).
35. P. Nieke *et al.*, *Materials* **12**, 487 (2019).
36. M.-Y. Cho *et al.*, *Electron. Mater. Lett.* **32**, 11 (2019).
37. Y. Hasegawa *et al.*, *J. Ceram. Soc. Jpn.* **125**, 482 (2017).
38. M. Schubert *et al.*, *Funct. Mater. Lett.* **12**, 1950039 (2019).
39. M. Schubert *et al.*, *Sensors* **19**, 1632 (2019).
40. M. Schubert *et al.*, *Materials* **7**, 5633 (2014).
41. S. D. Johnson *et al.*, *Proc. SPIE* **8708**, 87080T (2013).
42. C. Li *et al.*, *Int. J. Heat Mass Transfer* **129**, 1161 (2019).
43. A. Z. Yeganeh *et al.*, *Surf. Coat. Technol.* **370**, 269 (2019).
44. G. Mauer, *J. Therm. Spray Technol.* **17**, 115 (2018).
45. H. Park *et al.*, *J. Therm. Spray Technol.* **26**, 1616 (2017).
46. P. Sarobol *et al.*, *J. Therm. Spray Technol.* **25**, 82 (2016).
47. M. Bektas *et al.*, *J. Sens. Sens. Syst.* **3**, 223 (2014).

48. K. Sahner et al., *Sens. Actuators, B* **139**, 394 (2009).
49. C.-C. Hsiao et al., *Sensors* **14**, 12219 (2014).
50. A. Kumar et al., Patterning and annealing effects of aerosol deposited hygroscopic films for humidity sensors, in *2018 IEEE SENSORS*, IEEE, October 2018, pp. 1–4.
51. J.-G. Liang et al., *Sens. Actuators, B* **265**, 632 (2018).
52. H. Kim et al., *Sens. Actuators, B* **274**, 331 (2018).
53. G. Hagen et al., *Sens. Actuators, B* **236**, 1020 (2016).
54. G. Hagen et al., *Procedia Eng.* **120**, 241 (2015).
55. D. Hanft et al., *Materials* **11**, 1342 (2018).
56. M. Bektas et al., *Solid State Ion.* **316**, 1 (2018).
57. J. Ryu et al., *J. Am. Ceram. Soc.* **92**, 3084 (2009).
58. J. Ryu et al., *J. Appl. Phys.* **109**, 113722 (2011).
59. C.-W. Baek et al., *Kor. J. Mater. Res.* **21**, 277 (2011).
60. J. Ryu et al., *J. Nanosci. Nanotechnol.* **13**, 3422 (2013).
61. J.-E. Kang et al., *J. Alloys Compd.* **534**, 70 (2012).
62. H.-R. Jung et al., *J. Nanosci. Nanotechnol.* **15**, 2409 (2015).
63. M. Schubert et al., *Sensors* **18**, 3982 (2018).
64. M. Schubert et al., *Funct. Mater. Lett.* **10**, 1750073 (2017).
65. G. D. C. Csete de Györgyfalva et al., *J. Eur. Ceram. Soc.* **19**, 857 (1999).
66. R. Schmidt et al., *J. Eur. Ceram. Soc.* **24**, 1233 (2004).
67. R. Schmidt et al., *J. Eur. Ceram. Soc.* **23**, 1549 (2003).
68. J. Akedo et al., *Appl. Phys. Lett.* **77**, 1710 (2000).
69. W. Heywang et al., *Piezoelectricity* (Springer, Berlin, 2008).
70. J. Akedo et al., *J. Cryst. Growth* **235**, 415 (2002).
71. B.-D. Hahn et al., *J. Mater. Res.* **23**, 226 (2008).
72. H. Palneedi et al., *Appl. Phys. Lett.* **107**, 12904 (2015).
73. H. Palneedi et al., *Adv. Mater.* **29**, 1605688 (2017).
74. G.-T. Hwang et al., *Adv. Energy Mater.* **6**, 1600237 (2016).
75. W. D. Kingery et al., *Introduction to Ceramics* (Wiley, New York, 1976).
76. J. Robertson et al., *MRS Proc.* **361**, 1669 (1994).
77. Y. H. Do et al., *Sens. Actuators, A* **184**, 124 (2012).
78. J. Akedo et al., Aerosol deposition (AD) and its applications for piezoelectric devices, in *Advanced Piezoelectric Materials*, Chap. 15 (Elsevier, 2017), pp. 575–614.
79. J. Hwang et al., *Catal. Commun.* **94**, 1 (2017).
80. N. Asai et al., Novel high resolution optical scanner actuated by aerosol deposited PZT films, *Proc. IEEE Int. Conf. Micro Electro Mechanical Systems (MEMS)* (2003), pp. 247–250.
81. J.-H. Park et al., *Sens. Actuators, A* **135**, 86 (2007).
82. J. Akedo et al., *Jpn. J. Appl. Phys.* **44**, 7072 (2005).
83. J. Jung et al., *Appl. Phys. Lett.* **110**, 212903 (2017).
84. M. H. Kwak et al., *J. Ceram. Process. Res.* **18**, 731 (2017).
85. S. Baba et al., *J. Alloys Compd.* **589**, 56 (2014).
86. S. Baba et al., *J. Phys.: Conf. Ser.* **379**, 12011 (2012).
87. T. Stöcker et al., *Materials* **11**, 1888 (2018).
88. J. Akedo, *Mater. Sci. Forum* **449–452**, 43 (2004).
89. S. Hirose et al., Superconducting MgB<sub>2</sub> thick films by AD process, *Proc. 4<sup>th</sup> Tsukuba Int. Coatings Symposium — Frontiers of Coatings Technology: Innovative Processes and Applications* (2010), pp. 17–18.
90. S. Kauffmann-Weiss et al., *IEEE Trans. Appl. Supercond.* **27**, 6200904 (2017).
91. B. B. Sinha et al., *J. Supercond. Novel Magn.* **26**, 1507 (2013).
92. B. B. Sinha et al., *Prog. Supercond.* **13**, 122 (2011).
93. T. Arndt, Method and arrangement for producing superconducting layers on substrates, US2013/0123112A1 (16.05.2011).
94. C. Buzea et al., *Supercond. Sci. Technol.* **14**, R115 (2001).
95. J. Ramanujam et al., *Energy Environ. Sci.* **10**, 1306 (2017).
96. J.-J. Park et al., *Comput. Mater. Sci.* **101**, 66 (2015).
97. J.-J. Park et al., *Acta Mater.* **123**, 44 (2017).
98. W. A. Dunlap-Shohl et al., *Chem. Rev.* **119**, 3193 (2019).
99. D. Prochowicz et al., *J. Mater. Chem. A* **3**, 20772 (2015).
100. D. Andre et al., *J. Mater. Chem. A* **3**, 6709 (2015).
101. J. Janek et al., *Nat. Energy* **1**, 16141 (2016).
102. J. Schnell et al., *J. Power Sources* **382**, 160 (2018).
103. J. Schnell et al., *Energy Environ. Sci.* **23**, 1933 (2019).
104. R. Inada et al., *Front. Energy Res.* **4**, 336 (2016).
105. R. Inada et al., *J. Power Sources* **253**, 181 (2014).
106. T. Placke et al., *J. Solid State Electrochem.* **21**, 1939 (2017).
107. D. Popović et al., *J. Am. Ceram. Soc.* **94**, 3847 (2011).
108. A. Khan et al., *Met. Mater. Int.* **20**, 399 (2014).
109. R. Inada et al., *Ceram. Int.* **41**, 11136 (2015).
110. J.-J. Choi et al., *J. Korean Phys. Soc.* **68**, 12 (2016).
111. R. Inada et al., *Prog. Nat. Sci.: Mater. Int.* **27**, 350 (2017).
112. C.-W. Ahn et al., *J. Electrochem. Soc.* **162**, A60 (2014).
113. S. Takai et al., *Electrochemistry* **76**, 293 (2008).
114. I. Kim et al., *Nanoscale Res. Lett.* **7**, 64 (2012).
115. S. Iwasaki et al., *J. Power Sources* **272**, 1086 (2014).
116. C.-W. Ahn et al., *Carbon* **82**, 135 (2015).
117. I. Kim et al., *J. Power Sources* **244**, 646 (2013).
118. R. Inada et al., *Materials* **11**, 1570 (2018).
119. T. Kato et al., *J. Power Sources* **303**, 65 (2016).
120. M. Zarabian et al., *J. Electrochem. Soc.* **164**, A1133 (2017).
121. S. Lobe et al., *J. Power Sources* **307**, 684 (2016).
122. E. Fuchita et al., *J. Ceram. Soc. Jpn.* **118**, 767 (2010).
123. J. Akedo et al., *Jpn. J. Appl. Phys.* **40**, 5528 (2001).
124. S. Baba et al., *J. Am. Ceram. Soc.* **89**, 1736 (2006).
125. M. W. Lee et al., *J. Aerosol Sci.* **42**, 771 (2011).
126. Y. Imanaka, *J. Ceram. Sci. Technol.* **6**, 291 (2015).
127. D. H. Kim et al., Method for manufacturing all solid electrode having solid electrolyte concentration gradient, US2015/0340741A1 (14.12.2014).
128. L. Miara et al., *ACS Appl. Mater. Interfaces* **8**, 26842 (2016).
129. J.-J. Choi et al., *Int. J. Hydrog. Energy* **37**, 9809 (2012).
130. S.-F. Wang et al., *J. Power Sources* **196**, 5064 (2011).
131. B.-G. Seong et al., Anode supported SOFC with GDC barrier layer deposited by aerosol deposition method, *Proc. ASME 2010 8th Int. Fuel Cell Science, Engineering and Technology* (2010), pp. 351–357.
132. J.-J. Choi et al., *Int. J. Hydrog. Energy* **37**, 6830 (2012).
133. A. Billard et al., *C. R. Phys.* **19**, 755 (2018).
134. A. Vardelle et al., *J. Therm. Spray Technol.*, **25**, 1376 (2016).